Catalysis Science & Technology

PAPER

View Article Online
View Journal | View Issue

Cite this: *Catal. Sci. Technol.*, 2018, **8**, 4390

Water oxidation by a manganese–potassium cluster: Mn oxide as a kinetically dominant "true" catalyst for water oxidation†

Younes Mousazade,[a] Mohammad Reza Mohammadi,[bc] Petko Chernev,[bd] Rahman Bikas,*[e] Robabeh Bagheri,[f] Zhenlun Song,[f] Tadeusz Lis,[g] Holger Dau[b] and Mohammad Mahdi Najafpour*[ahi]

Received 4th June 2018,
Accepted 22nd July 2018

DOI: 10.1039/c8cy01151f

rsc.li/catalysis

Nature uses an Mn cluster for water oxidation, and thus, water oxidation using Mn clusters is interesting when used in artificial water-splitting systems. An important question is whether an Mn cluster is a true catalyst for water oxidation or not. Herein, an Mn–K cluster was investigated for electrochemical water oxidation to find the true and the kinetically dominant catalyst using X-ray absorption spectroscopy, scanning electron microscopy, transmission electron microscopy, Fourier transform infrared spectroscopy, X-ray diffraction, and electrochemical methods. The experiments showed that conversion into nanosized Mn oxide occurred for the cluster, and the nanosized Mn oxides are the true catalyst for water oxidation.

Introduction

The design and synthesis of an efficient and stable water-oxidizing catalyst are big challenges in science and technology.[1–9] An interesting part of the photosystem II reaction center in oxygenic photosynthetic organisms is the oxygen-evolving complex (OEC) or water-oxidizing complex (WOC).[10–13] The WOC contains a $CaMn_4O_5(H_2O)_4$ cluster, which accumulates four oxidizing equivalents from four photochemical reactions. The structure is a significant development by nature for the ability of storing oxidizing equivalents.[10–13] This is necessary because water oxidation is a four-electron process, but photochemistry is a one-electron process.[10–13] The $CaMn_4O_5$ cluster is coordinated by four water molecules, six carboxylate groups and one imidazole of the amino acid residues. The Mn_4CaO_5 cluster is the only known system to catalyze water oxidation in nature.[10–13] Recently, a structural model for the site has been reported.[14]

Mn compounds are very interesting when used as water-oxidizing catalysts. In 1974, Calvin reported $[(bpy)_2Mn^{III}(\mu\text{-}O)_2Mn^{IV}(bpy)_2]^{3+}$ for water splitting and photosynthetic solar energy conversion.[15] Mononuclear Mn complexes are rarely reported for water oxidation.[16–19]

The Smith group reported Mn(II)–pyridinophane complexes $[(Py_2NR_2)Mn(H_2O)_2]^{2+}$ (R = H, Me, *t*-Bu) for the formation of O_2.[16] The complex with bulky substituents (R = *t*-Bu) has catalytic activity for water oxidation.[16] Mn^{III} complexes of the type $[MnL(H_2O)]^{2+}$, L: Schiff base ligand, have been shown to induce water oxidation under different conditions,[17,18] but, the true catalyst for water oxidation was not known.

Dimeric tetraarylporphyrins with water-oxidizing activity at potentials greater than 1.20 V *vs.* Ag/Ag^+ were reported.[20,21] $[(OH_2)(terpy)Mn(\mu\text{-}O)_2Mn(terpy)(OH_2)]^{3+}$ (terpy: 2,2′:6′,2″-terpyridine), an important compound introduced in 1999, is one of the most important Mn-based complexes for water oxidation in the presence of HSO_5^- or ClO^-.[22,23] A dinuclear Mn complex with imidazole groups has also been reported with water-oxidizing activity.[24]

A series of $Mn_{12}O_{12}(OAc)_{16-x}L_x(H_2O)_4$ (L = acetate, benzoate, benzenesulfonate, diphenylphosphonate, and

[a] *Department of Chemistry, Institute for Advanced Studies in Basic Sciences (IASBS), Zanjan, 45137-66731, Iran. E-mail: mmnajafpour@iasbs.ac.ir; Tel: Phone: (+98) 24 3315 3201*
[b] *Fachbereich Physik, Freie Universität Berlin, Arnimallee 14, 14195 Berlin, Germany*
[c] *Department of Physics, University of Sistan and Baluchestan, Zahedan, 98167-45845, Iran*
[d] *Department of Chemistry - Ångströmlaboratoriet, Uppsala University, Lägerhyddsvägen 1, 75120 Uppsala, Sweden*
[e] *Department of Chemistry, Faculty of Science, Imam Khomeini International University, 34148-96818, Qazvin, Iran. E-mail: bikas@sci.ikiu.ac.ir*
[f] *Surface Protection Research Group, Surface Department, Ningbo Institute of Materials Technology and Engineering, Chinese Academy of Sciences, 519 Zhuangshi Road, Ningbo 315201, China*
[g] *Faculty of Chemistry, University of Wroclaw, Joliot-Curie 14, 50-383 Wroclaw, Poland*
[h] *Center of Climate Change and Global Warming, Institute for Advanced Studies in Basic Sciences (IASBS), Zanjan, 45137-66731, Iran*
[i] *Research Center for Basic Sciences & Modern Technologies (RBST), Institute for Advanced Studies in Basic Sciences (IASBS), Zanjan 45137-66731, Iran*

† Electronic supplementary information (ESI) available. CCDC 1844199 contains the supplementary crystallographic data for **1**. For ESI and crystallographic data in CIF or other electronic format see DOI: 10.1039/c8cy01151f

dichloroacetate) was reported.[25] These clusters were studied as catalysts for water oxidation on a fluorine-doped tin oxide glass electrode (FTO). Four $[Mn_{12}O_{12}]$ compounds showed water oxidation activity at pH 7.0, 640–820 mV with 0.2 mA cm^{-2} and high Faradaic efficiency (85–93%). More than 200 turnovers were observed after 5 minutes for the most active complex. The research group proposed that these complexes need at least a one-electron oxidation to become active catalysts. A greater degree of distortion at two Mn ions in the structure also correlated with the higher catalytic activity.[25]

Agapie's group reported tetranuclear manganese complexes featuring three six-coordinated and one five coordinated Mn centers displaying hydrogen bonding networks as more accurate structural models of the biological water oxidation. These species support electrocatalytic water oxidation to H_2O_2, albeit in low yield.[26]

Recently, Maayan's and Christou's groups reported the synthesis and characterization of $[Mn_{12}O_{12}(O_2CC_6H_3(OH)_2)_{16}(H_2O)_4]$.[27] The authors reported the complex as a unique example of this class of compounds because of its high solubility and stability in water.[27] The research groups indicated that the cluster is a stable homogeneous water-oxidizing electrocatalyst operating at pH 6 with an exceptionally low overpotential of only 334 mV.[27]

Finding the kinetically dominant catalysts in different reactions is a challenge. Finding the true catalyst in a reaction can be important for the design and synthesis of efficient and stable catalysts for the said reaction. In some cases, the evidence showed that some Mn complexes and salts under different reduction and oxidation reactions are not stable and decompose to Mn oxide,[28–31] which in some cases is the true catalyst. However, understanding "what is the true catalyst" under oxidation or reduction conditions is a challenge. From a molecular orbital theory (MOT) side and based on a simple view, adding and removing electron(s) from a metal complex causes changes depending on the bonding, antibonding or non-bonding character of the frontier orbitals of the complex. Such changes destabilize the complexes because removing electron(s) from the highest occupied molecular orbital (HOMO), which usually possesses bonding character, can weaken the framework of the complexes. On the other hand, adding electron(s) to the lowest unoccupied molecular orbital (LUMO), which usually has anti-bonding character can also weaken the framework.[32] Therefore, it is not surprising that usually the highly oxidized or reduced complexes are unstable toward decomposition. The products of decomposition and details of such decompositions were not usually investigated.

Herein, an Mn–K cluster (**1**) was synthesized, characterized and investigated under electrochemical water-oxidation conditions. By several methods, we showed that for such a cluster, conversion into nanosized Mn oxide occurs during the water-oxidation reaction. Our experiments showed that such nanosized Mn oxides are the true catalyst for water oxidation.

Experimental

Materials and instrumentation

$KMnO_4$ (Sigma-Aldrich Company, assay ≥99.0%), Nafion (5%; Sigma-Aldrich Company), $Mn(OAc)_2{\cdot}4H_2O$ (Sigma-Aldrich Company, ≥99%) and pivalic acid (Sigma-Aldrich Company, assay = 99%) were purchased and used as received. The solvents (Aldrich Company) were used without further purification.

Instrumentation

TEM was carried out using an FEI Tecnai G^2 F20 transmission electron microscope (TF20 200 kV). SEM and EDX were carried out using a VEGA\TESCAN-XMU. The X-ray powder patterns were recorded with a Bruker D8 ADVANCE (Germany) diffractometer (CuK_α radiation). The infrared spectra were obtained on a FT-IR Bruker Vector spectrometer using a pressed KBr pellet. Electrochemical experiments were performed using an $EmStat^{3+}$ from PalmSens Company (the Netherlands). Fluorine-doped tin oxide (FTO) and Pt foil were the working and the auxiliary electrodes, respectively. The elemental analysis (carbon, hydrogen and nitrogen) results were obtained using a Carlo ERBA Model EA 1108 analyzer.

Synthesis of $[Mn_8K_2(\mu\text{-}O)_4(\mu\text{-}OH)_2(Piv)_{16}(Piv{-}H)(CH_3CN)]{\cdot}CH_3COOH$ (1)

1 was synthesized by the reaction of $KMnO_4$ (0.158 g, 1.00 mmol), $Mn(OAc)_2{\cdot}4H_2O$ (0.735 g, 3.00 mmol) and pivalic acid (0.511 g, 5.00 mmol) in acetonitrile (20 mL). The mentioned amounts of the materials were placed in the main arm of a branched tube. The solvent was carefully added to fill the arms and the tube was sealed. The reagent containing arm was immersed in an oil bath at 65 °C, while the other arm was kept at ambient temperature. After one day, dark-red plate crystals were deposited in the cooler arm. After two days, the crystals were isolated from the tube, washed with cold acetonitrile and dried at room temperature. Yield (based on Mn) ≈70% (0.84 g). Anal. calc. for $C_{84}H_{153}K_2Mn_8NO_{40}{\cdot}C_2H_4O_2$ (MW = 2394.84): C, 43.13; H, 6.61; N, 0.58; K, 3.27; Mn, 18.35. Found: C, 43.39; H, 6.68; N, 1.19; K, 3.29; Mn, 18.54%. FT-IR (KBr, cm^{-1}): 3429 (br, s), 2961 (s), 2930 (m), 2873 (m), 1699 (m), 1594 (vs), 1470 (s), 1555 (s), 1531 (m), 1483 (vs), 1459 (m), 1413 (vs), 1359 (s), 1329 (m), 1226 (s), 1031 (w), 937 (w), 894 (w), 870 (w), 789 (w), 614 (vs), 590 (s), 511 (s), 430 (vs).

Single crystal X-ray structural analysis

The dark-red plate crystals of **1** were obtained from CH_3CN by the thermal gradient method. The crystals of **1** crystallized in the monoclinic space group $P2_1/n$. The X-ray data were collected at 80 K using an Xcalibur, Ruby diffractometer with MoK_α radiation λ = 0.71073 Å. Analytical absorption correction was applied with maximum and minimum transmissions of 0.797 and 0.947.[33] The structure was solved by direct methods using SHELXS97 (ref. 34) and refined with the full-matrix least-squares method on F^2 with the use of the SHELX-2014 program package.[35] The hydrogen atoms have

been located from the difference electron density maps and constrained during refinement. The data collection and refinement processes are summarized in Table S1.† The selected bond lengths, angles and characters for the hydrogen bonds are presented in Tables 1, S2 and S3,† respectively.

Cyclic voltammetry

For the investigation of the electrochemical behavior of **1**, cyclic voltammetry (CV) in a three-electrode cell was performed in which Ag/AgCl, a platinum sheet and FTO were used as the reference, the counter and the working electrodes, respectively. 3.0 mg (1.25 μmol) of **1** was added to 30 mL water and dispersed by sonication. Cyclic voltammetry was performed in the range of −0.2 to 1.6 V (*vs.* Ag/AgCl) at room temperature at a 50 mV s^{-1} scan rate in phosphate buffer (1.0 M, pH = 6.7). 50 cycles of measurement were made to follow the cluster behavior in long time operation. The same measurement was performed for FTO without **1**.

Amperometry

3.0 mg (1.25 μmol) of **1** was added to 30 mL water and dispersed by sonication, and then, this dispersed mixture (30 μL) was dropped on an FTO electrode (1.0 cm^2) and dried at ambient temperature. The amperometry measurement at 1.4 V was performed in a solution of phosphate buffer (1.0 M, pH = 6.7) and by using Ag/AgCl and a platinum sheet as the reference and auxiliary electrodes, respectively.

Such electrodes were used for the SEM experiments. The mechanically separated solid from the FTO electrode was used for TEM, FT-IR and XRD experiments. The same procedure was repeated for a bare FTO electrode for comparison with the water oxidation activity of **1**.

XAS measurements

3.0 mg (1.25 μmol) of **1** was added to 30 mL of water and dispersed by sonication, and then, this dispersed mixture (30 μL) was dropped on an FTO electrode (1.0 cm^2) and dried at ambient temperature. The amperometry measurement at 1.4 V for two hours was performed in a solution of phosphate buffer (1.0 M, pH = 6.7) and by using Ag/AgCl and a platinum sheet as the reference and auxiliary electrodes, respectively. XAS measurements (EXAFS, XANES) at the manganese K-edges for the obtained sample after amperometry and for a sample before amperometry were performed at the KMC-3 beamline at the BESSY II synchrotron facility (Helmholtz-Zentrum Berlin, Germany) at 20 K in a liquid-helium cooled cryostat (Oxford-Danfysik). The measurements were performed in the top-up mode of the BESSY II storage ring, at a 250 mA ring current.

The angle between the sample surface and the incident beam was approximately 45°. Fluorescence-detected X-ray absorption spectra at the manganese K-edge were collected using a 13-element Ge detector (Ultra-LEGe detector, Canberra GmbH) installed perpendicular to the incident X-ray beam.

Oxygen evolution measurements

The oxygen evolution measurements were carried out at 25.0 °C using an optical-probe oxygen meter (HQ40d from Hach

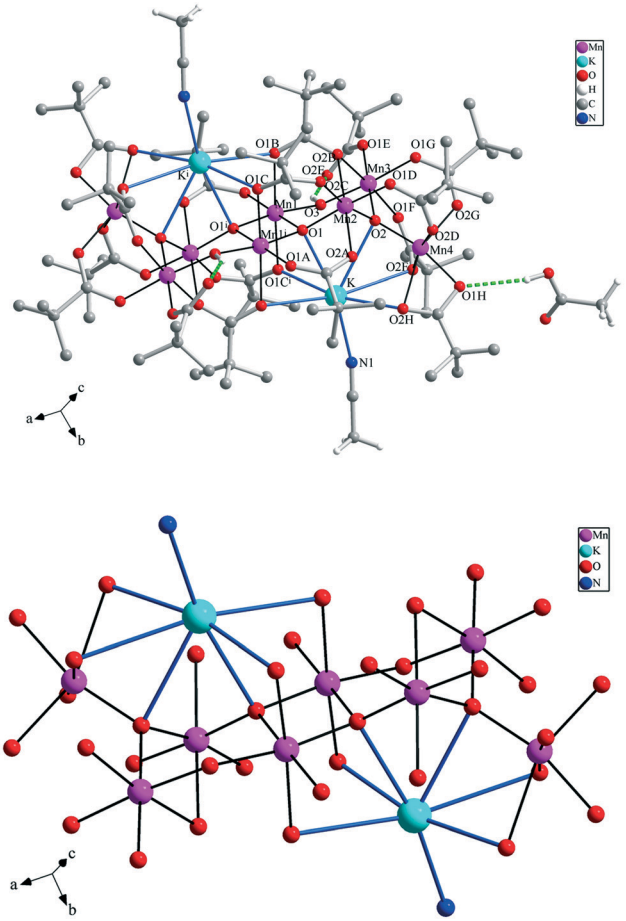

Fig. 1 The molecular structure of **1**; *i* = −*x* + 1, −*y*, −*z* + 1. The hydrogen atoms of the $-CH_3$ groups for pivalic acid and the disordered atoms are omitted for clarity. The green dashed lines show O–H···O hydrogen bonds.

Table 1 Selected bond lengths around the Mn(III) ions for **1**

Bond	Length (Å)	Bond	Length (Å)
Mn1–Mn1^{i}	2.8575(15)	Mn2–Mn3	3.1019(15)
Mn2–Mn3	3.1090(18)	Mn3–Mn4	3.2781(15)
Mn1–O1	1.881(3)	Mn3–O3^{i}	1.896(3)
Mn1–O1^{i}	1.908(3)	Mn3–O1E	1.929(3)
Mn1–O3	1.929(3)	Mn3–O2	1.930(3)
Mn1–O1A	1.953(3)	Mn3–O1G	1.944(3)
Mn1–O1B	2.252(3)	Mn3–O1F	2.144(3)
Mn1–O1C	2.258(3)	Mn3–O2B^{i}	2.231(3)
Mn2–O2	1.896(3)	Mn4–O2	1.864(3)
Mn2–O1	1.906(3)	Mn4–O2D	1.940(3)
Mn2–O2C	1.945(3)	Mn4–O2F	1.947(3)
Mn2–O1D	1.950(3)	Mn4–O1H	1.963(3)
Mn2–O2A	2.150(3)	Mn4–O2G	2.118(3)
Mn2–O2B^{i}	2.209(3)	Mn4–O2H	2.356(3)

Symmetry code: (i) −*x* + 1, −*y*, −*z* + 1.

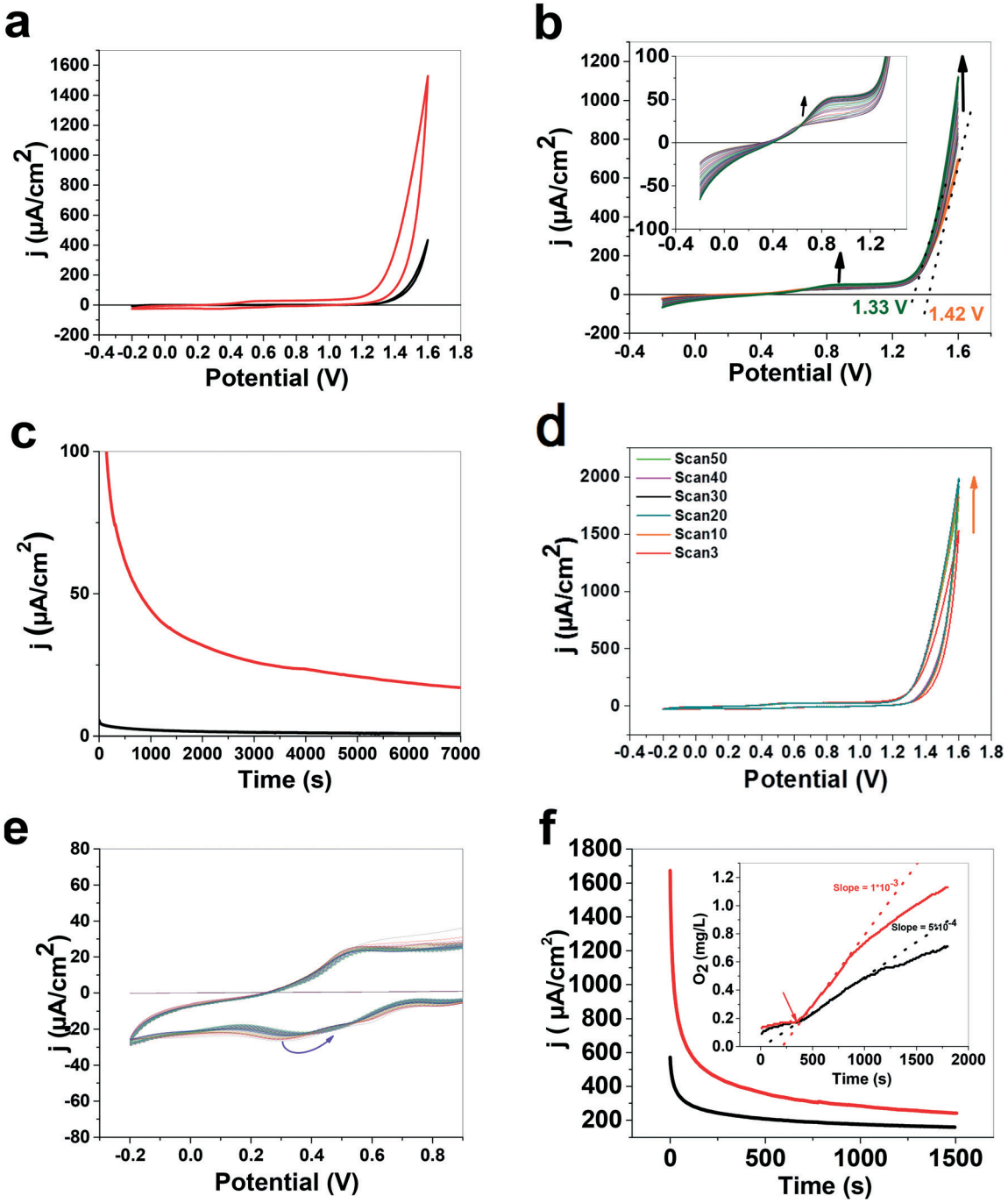

Fig. 2 Comparison of CV results for **1** in 25.0 mL of phosphate buffer (1.0 M, pH = 6.7) (cycle no = 35; red) and phosphate buffer in the absence of the cluster (black) (a). Continuous LSV measurements for **1** in 25.0 mL of phosphate buffer (1.0 M, pH = 6.7) (LSV no 1 (orange) and LSV no 100 (dark green) with overpotentials of 790 and 700 mV, respectively) (b). Comparison of the water-oxidation activity of FTO in the presence (red) and absence (black) of **1** *via* amperometry at 1.4 V for 2 h (c). 50 CV measurements of **1** on FTO in 25.0 mL of phosphate buffer (1.0 M, pH = 6.7) (d). Expanded range of the 50 CV measurements to visualize Mn redox peaks in the −0.2 to 1.4 area (e). Oxygen evolution/amperometry of **1** (red) and a fresh FTO electrode (black) at 1.8 V (f). In all the cases, the reference and counter electrodes were Ag/AgCl and a Pt sheet, respectively.

Company, Düsseldorf, Germany) *via* amperometry in 1.4 V *vs.* the Ag/AgCl reference electrode with and without of **1** on the FTO electrode in phosphate buffer (1.0 M, pH = 6.7). In each case, the potential was applied after 5 min of oxygen evolution measurements.

Results and discussion

Syntheses and spectroscopy

The facile reaction of $KMnO_4$ with $Mn(OAc)_2{\cdot}4H_2O$ and pivalic acid in acetonitrile afforded **1**. **1** was characterized by

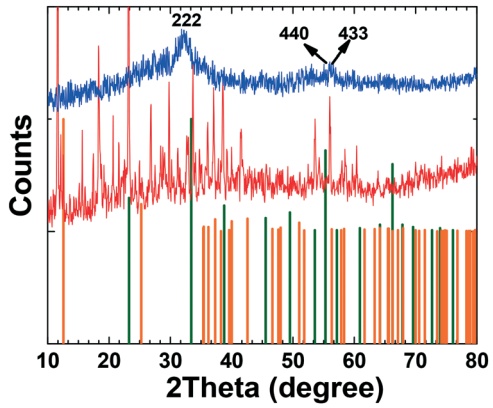

Fig. 3 XRD patterns of **1** before (red) and after (blue) the amperometry at 1.4 V for 2 h in 25.0 mL of phosphate buffer (1.0 M, pH = 6.7) (Mn_2O_3 (ref. code: 00-001-1061): green; birnessite (ref. code 01-080-1098): orange).

elemental analysis, spectroscopic methods, and single crystal X-ray analysis.

X-ray structure of 1

The single-crystal X-ray structural analysis shows that **1** is a neutral octanuclear Mn(III) complex which also contains two K(I) ions. A perspective view of the molecular structure with an atom numbering scheme is shown in Fig. 1, and selected bond lengths and angles relevant to the Mn(III) coordination sphere are listed in Tables 1 and S2.† The single crystal X-ray structure of the plate red crystals of **1** revealed that the asymmetric unit of the crystal packing contains half of the complex, wherein the other half is generated by symmetry inversion. All of the manganese ions in this complex are Mn(III) ions which are connected together by the oxygen atoms of carboxylate groups and oxide-bridging ligands. The Mn···Mn distances are in the range of 2.855–3.492 Å. All Mn(III) ions have a distorted octahedral coordination environment and show a Z-out Jahn–Teller effect which is usually seen in Mn(III) ions with an HS-d^4 electron configuration. The μ-O(H) groups are coordinated to three Mn(III) and one K ions and have distorted tetrahedral geometry. The μ-O(H) groups act as a bridge between the Mn1 and Mn3 ions and form strong intramolecular hydrogen bonds with the oxygen atoms of the coordinated pivalate ligand (Table S2†). The carboxylate groups connect the metal ions in μ-1,3, μ-1,1,3 and μ-1,1,3,3 bridging modes. The potassium ion is also connected to the Mn(III) ions by six oxygen atoms of the carboxylate and oxide groups.

Electrochemical studies

The CV and LSV results of **1** are shown in Fig. 2a and b, which indicates that compared to a fresh FTO electrode, water-oxidation activity was observed by adding **1** to the FTO electrode after some CV or LSV measurements. The overpotential for the onset of water oxidation under these conditions is 700 mV. The fresh FTO under the same conditions, but in the absence of **1** (Fig. S1†) showed lower activity for water oxidation (overpotential for the onset of water oxidation: 790 mV). Repeated LSV measurements showed an increase in the water oxidation. This could indicate the decomposition of **1** under water oxidation toward a water-oxidizing catalyst.

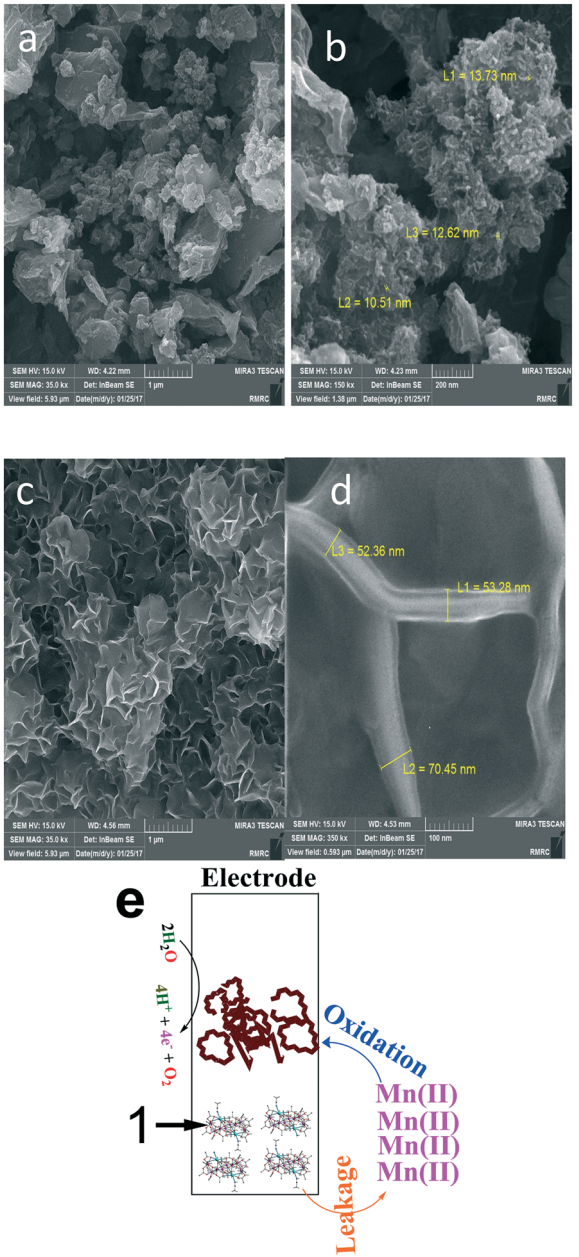

Fig. 4 SEM images of **1** before (a and b) and after (c and d) amperometry at 1.4 V for 2 h in 25.0 mL of phosphate buffer (1.0 M, pH = 6.7). The schematic image shows a proposed conversion of Mn oxide by the decomposition of **1** (e). Under the water oxidation, leaking of Mn(II) ions, which resulted from the water-oxidation reaction or disproportions of Mn(III), and re-oxidizing of these Mn(II) ions could convert **1** to Mn oxide.

The repeated LSV measurements indicated a new peak at 0.8 V attributed to Mn oxidation of the Mn oxides.[36] The effect of the activation of **1** in the water-oxidation reaction was

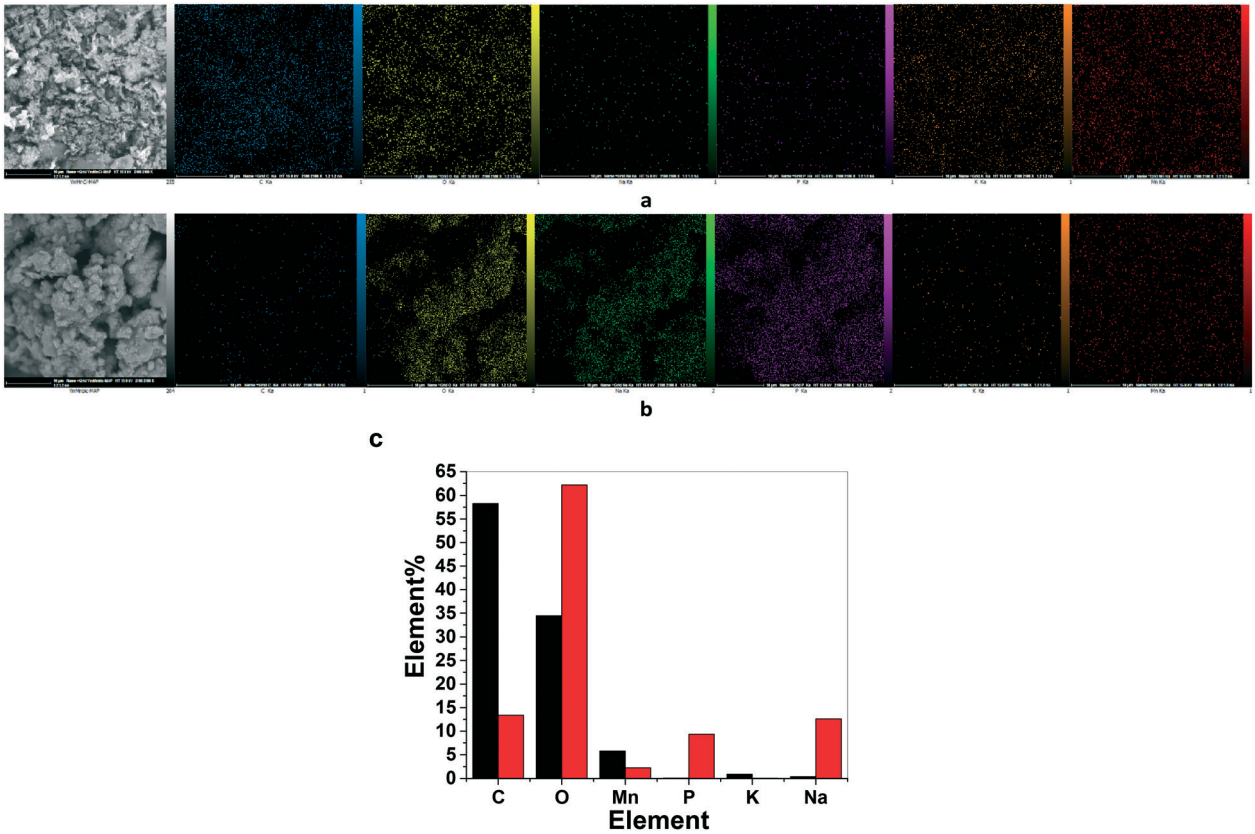

Fig. 5 EDX-map of **1** before (a) and after (b) amperometry at 1.4 V for 2 h in 25.0 mL of phosphate buffer (1.0 M, pH = 6.7). Element ratio before (red) and after (black) amperometry at 1.4 V for 2 h in 25.0 mL of phosphate buffer (1.0 M, pH = 6.7) (C: blue; O: yellow; Na: green; P: purple; K: brown; Mn: red). The diagram shows the amounts of the element before (black) and after (red) the water-oxidation reaction on the surface of FTO (c).

also observed in the amperometry results (Fig. 2c). The rate of water oxidation by **1** was increased by continuous CV (Fig. 2d), which could show that the true catalyst may not have a molecular structure as that of **1**. The details of the CV results showed that the attributed oxidation peaks at 0.55 V showed a few changes under continuous CV (Fig. 2e). Significant changes from 0.30 to 0.45 V were observed with the attributed reduction peak under continuous CVs (Fig. 2e). The oxygen evolution/amperometry using **1** and a fresh electrode was compared in Fig. 2f. As shown in Fig. 2f, water oxidation in the presence of the cluster is two times higher than that using a fresh FTO electrode under similar conditions.

In the next step, we characterized the film on the FTO electrode using several methods. Comparing the XRD patterns for **1** before and after the water-oxidation reaction, significant changes were observed (Fig. 3). Although **1** is

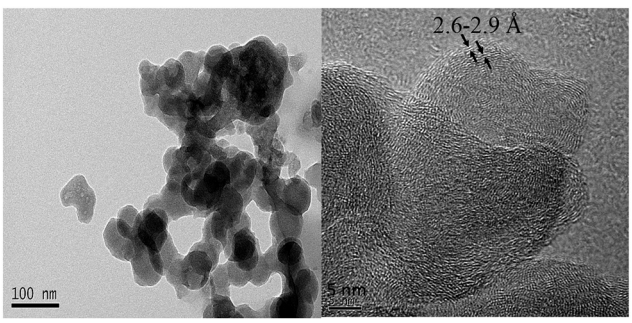

Fig. 6 (HR)TEM images of **1** after amperometry at 1.4 V for 2 h in 25.0 mL of phosphate buffer (1.0 M, pH = 6.7).

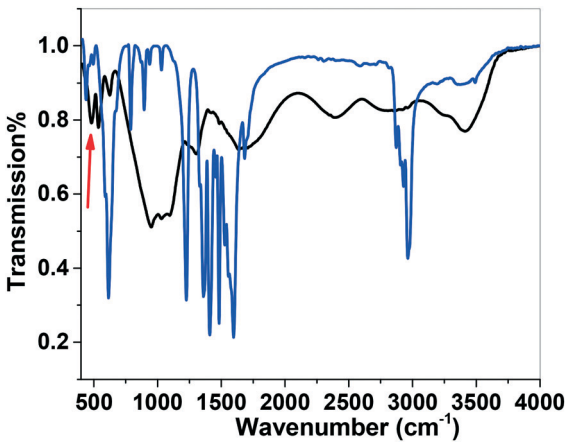

Fig. 7 FT-IR spectra of **1** before (blue) and after (black) amperometry at 1.4 V for 2 h in 25.0 mL of phosphate buffer (1.0 M, pH = 6.7). The red arrow shows the peak attributed to Mn–O–Mn.

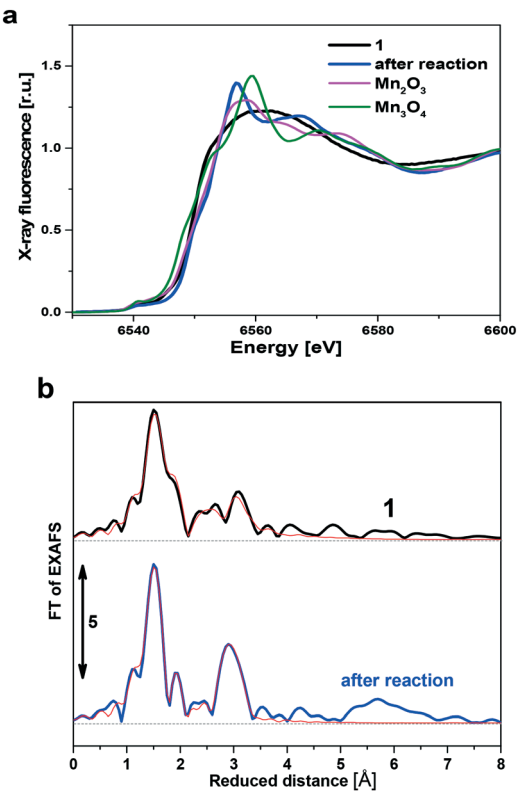

Fig. 8 XANES spectra (a) and Fourier-transform of the EXAFS spectra (b) of **1** (black) and the obtained compound after amperometry (blue) at 1.4 V for 2 h in phosphate buffer (1.0 M, pH = 6.7). The thick lines show experimental data, and the thin red lines show simulations. Phase shift not corrected. The k^3-weighted EXAFS oscillations are shown in Fig. S5.† The fit parameters for the simulations are given in Table 2.

crystalline with many peaks attributed to the different interplanar spacing in a molecular structure of **1**, after the water-oxidation reaction, it is converted to an amorphous compound with weak peaks that can be assigned to Mn_2O_3 (ref. code: 00-001-1061; crystal system: cubic space group: $Ia\bar{3}$; space group number: 206; $a = b = c$: 9.41 (Å); $\alpha = \beta = \gamma$: 90(°)). Mn_2O_3 is the phase different from the proposed one using the Pourbaix diagram by water oxidation,[37] which is Mn(IV) oxide. We hypothesize that under these conditions, high concentrations of the organic compound act as a solvent on the surface of FTO and inhibit the formation of high-valent Mn oxides (such as MnO_2). It was also reported that organic compounds in the presence of MnO_2 lower the oxidation state of Mn.[38]

The SEM images of **1** on FTO before the water-oxidation reaction showed thick layers, which are significantly aggregated and agglomerated forming particles (*ca.* 0.2–1 μm) (Fig. 4a and b; Fig. S2†). Each particle contains many amorphous nanoparticles (*ca.* 10–20 nm). However, after the water-oxidation reaction, a nanolayered morphology (thickness 50–80 nm) was observed on the surface of FTO (Fig. 4c and d; Fig. S3†). If we assume that the thickness of each monosheet is 1 nm, each nanolayer in the structure contains 50–80 monosheets. Such a morphology has usually been observed under leakage/oxidation processes.[36] Under these conditions, first leaking of Mn(II) from the disproportionation of Mn(III) occurs, which could be detected by atomic absorption spectroscopy. In the next step, re-oxidation of Mn(II) on the surface of FTO forms such nanolayers (Fig. 4e).

The EDX-SEM data from **1** showed that the compound contains (atomic) C (~58.29%), O (34.47%), Mn (~5.79%) and K (~0.92%). The formula of the surface of FTO in the presence of **1** can be written as $Mn_{6.3}KC_{63.3}O_{37.5}$. After the water-oxidation reaction, the EDX-SEM data from the obtained film contains O (62.18%), C (~13.39%), Na (~12.61%), P (~9.34%) and Mn (~2.27%). The formula of the surface of the electrode can be written as $MnNa_{5.5}P_{4.41}C_{5.9}O_{27.4}$ (Fig. 5). Thus, EDX results showed that the compound after the water-oxidation reaction is completely different from **1**. After the water-oxidation reaction, the amount of carbon decreased and the Na^+ and PO_4^{3-} from the buffer were found on the surface of the converted catalyst.

TEM images of the mechanically separated solid from the FTO after the water-oxidation reaction indicated a complicated morphology similar to that of a net system (Fig. 6; Fig. S4†). The HRTEM images indicated the lattice fringes with interplanar distances of 2.6–2.9 Å, which is consistent with the XRD results (2Θ = 30–34°). After the water-oxidation reaction, the low crystallinity of the compound could be observed in the HRTEM images (Fig. 6; Fig. S4†).

The FT-IR spectrum of **1** showed strong bands at 1500–1600 cm^{-1} which can be assigned to the C=O bond of carboxylate groups attributed to the organic ligand around the cluster (Fig. 7).[21] The broad peak around 3400 cm^{-1} confirms the presence of OH groups involved in hydrogen bond interactions.[21] Comparing the FT-IR spectra of **1** and that of the mechanically separated solid on FTO after the water-oxidation reaction showed that the organic ligand in

Table 2 Parameters obtained by the simulation of the k^3-weighted EXAFS spectra shown in Fig. 8. For **1**, the sum of the coordination numbers (CN) of the O shells was set to 6, and the sum of the Mn CN was set to 3.25, as suggested by the molecular structure. The energy shift (ΔE_0, −2.8 eV) and Debye–Waller parameters (σ, 0.058 Å and 0.033 Å for O and Mn, respectively) determined from this fit were then used for the simulation of the sample after the operation. The filtered R-factors were 16 and 14 for the initial complex and the operated one, respectively, and the reduced χ^2 values were 2.5 and 4.1. More details are given in the ESI

Sample		Mn–O	Mn–O	Mn–Mn	Mn–Mn	Mn–Mn
Initial complex (**1**)	Distance [Å]	1.91 ± 0.01	2.22 ± 0.01	2.81 ± 0.03	3.18 ± 0.01	3.33 ± 0.01
	Coordination number	3.8 ± 0.1	2.2 ± 0.1	0.2 ± 0.1	1.3 ± 0.1	1.7 ± 0.1
After the operation	Distance [Å]	1.93 ± 0.01	2.16 ± 0.01	2.91 ± 0.02	3.13 ± 0.01	3.45 ± 0.01
	Coordination number	4.3 ± 0.2	1.9 ± 0.3	0.4 ± 0.2	0.9 ± 0.2	1.0 ± 0.3

1 was removed after the water-oxidation reaction and a peak at 500–600 cm^{-1} attributed to Mn–O–Mn was observed.[39,40] On the other hand, the peaks attributed to carboxylates from pivalate at 1550–1610 cm^{-1} were not observed.[40]

In the next step, we used X-ray absorption spectroscopy (XAS) to get information about the conversion.

Fig. 8a shows that the Mn K-edge shifts from 6549.5 eV to 6550.6 eV during operation, which corresponds to the average Mn oxidation states of 2.9 and 3.2, respectively.[41] The shape of the edge also changes after the operation, and its structure becomes similar to that of a mixture of Mn_2O_3, Mn_3O_4 and MnO_2. A linear combination fit of the edge region using reference samples yields an average Mn oxidation state after the operation slightly higher than 3 (3.04).

The Fourier transform of the experimental EXAFS-spectrum of 1 can be readily reproduced by a simulation that directly uses its molecular structure (Fig. S6†). The spectrum shows a high main Mn–O peak that can be simulated by two Mn–O shells at 1.91 Å and 2.22 Å for 1 and Mn–O shells at 1.93 and 2.16 Å for the operated sample (Fig. 8b, Table 2). The spectrum of 1 has two broad Mn–Mn peaks with low amplitude, corresponding to di- and mono-μ-oxo bridged Mn; the two peaks merge after the operation, suggesting that the Mn–Mn distances become more uniform in length after the water oxidation reaction. This peak can be attributed to two main Mn–Mn distances of 3.13 Å and 3.45 Å, which is typical for manganese oxide, *e.g.* Mn_3O_4.

1 is an interesting model for the water-oxidizing complex in photosystem II. However, the instability of this structure under the water-oxidizing conditions shows that important strategies should be used to form a stable water-oxidizing cluster as nature uses it. It is clear that the polypeptide around the Mn cluster is important in stabilizing the attributed cluster in the biological system.[10–13] Although a very similar decomposition is known for photosystem II, nature uses a self-healing mechanism to heal the biological water-oxidizing cluster.[42]

Conclusions

In conclusion, by X-ray absorption spectroscopy, scanning electron microscopy, transmission electron microscopy, Fourier transform infrared spectroscopy, X-ray diffraction, and electrochemical methods, we showed that 1, although being a structural model for the water-oxidizing complex in photosystem II, under water-oxidation conditions is not a cluster-based catalyst for water oxidation. Under the water oxidation, 1 was decomposed to an Mn oxide which is the true catalyst for water oxidation. The challenge is whether a true Mn-based cluster as a water-oxidizing catalyst can be designed that offers a technological perspective. Such a cluster should have a very stable ligand. In addition to that, the cluster should oxidize water at a low overpotential to inhibit ligand oxidation. Alternatively, a metal cluster with a self-healing mechanism could be very promising.

Conflicts of interest

The authors declare no competing financial interests.

Acknowledgements

MMN and YM are grateful to the Institute for Advanced Studies in Basic Sciences and the National Elite Foundation for the financial support. RB thanks Imam Khomeini International University and the National Elite Foundation for the financial support. MRM, PC, and HD thank the Deutsche Forschungsgemeinschaft (DFG, Priority Programm SPP 1613, DA 402/7-2) and the Bundesministerium fuer Bildung und Forschung (BMBF, 05K16KE2 and 03SF0523B) for financial support. We thank the Helmholtz Zentrum Berlin (HZB) for allocation of beamtime and support at the KMC-3 beamline of the BESSY synchrotron.

Notes and references

1 M. Blasco-Ahicart, J. Soriano-López, J. J. Carbó, J. M. Poblet and J. Galan-Mascaros, *Nat. Chem.*, 2018, **10**, 24.
2 M. D. Kärkäs, O. Verho, E. V. Johnston and B. Åkermark, *Chem. Rev.*, 2014, **114**, 11863–12001.
3 J. P. McEvoy and G. W. Brudvig, *Chem. Rev.*, 2006, **106**, 4455–4483.
4 M. M. Najafpour, G. Renger, M. Hołyńska, A. N. Moghaddam, E.-M. Aro, R. Carpentier, H. Nishihara, J. J. Eaton-Rye, J.-R. Shen and S. I. Allakhverdiev, *Chem. Rev.*, 2016, **116**, 2886–2936; M. M. Najafpour, M. Hołyńska and S. Salimi, *Coord. Chem. Rev.*, 2015, **285**, 65–75.
5 W. Rüttinger and G. C. Dismukes, *Chem. Rev.*, 1997, **97**, 1–24.
6 M. G. Walter, E. L. Warren, J. R. McKone, S. W. Boettcher, Q. Mi, E. A. Santori and N. S. Lewis, *Chem. Rev.*, 2010, **110**, 6446–6473.
7 M. Wiechen, M. Najafpour, S. Allakhverdiev and L. Spiccia, *Energy Environ. Sci.*, 2014, **7**, 2203–2212.
8 M. Yagi and M. Kaneko, *Chem. Rev.*, 2001, **101**, 21–36.
9 K. J. Young, B. J. Brennan, R. Tagore and G. W. Brudvig, *Acc. Chem. Res.*, 2015, **48**, 567–574.
10 R. E. Blankenship, *Molecular mechanisms of photosynthesis*, John Wiley & Sons, 2014.
11 K. N. Ferreira, T. M. Iverson, K. Maghlaoui, J. Barber and S. Iwata, *Science*, 2004, **303**, 1831–1838; J. Barber, *Chem. Soc. Rev.*, 2009, **38**, 185–196; J. Barber, *Biochemistry*, 2016, **55**, 5901–5906; J. Barber, *Nat. Plants*, 2017, **3**, 17041.
12 M. Suga, F. Akita, K. Hirata, G. Ueno, H. Murakami, Y. Nakajima, T. Shimizu, K. Yamashita, M. Yamamoto, H. Ago and J. R. Shen, *Nature*, 2015, **517**, 99; H. Ago, H. Adachi, Y. Umena, T. Tashiro, K. Kawakami, N. Kamiya, L. Tian, G. Han, T. Kuang, Z. Liu, F. Wang, H. Zou, I. Enami, M. Miyano and J.-R. Shen, *J. Biol. Chem.*, 2016, **291**, 5676–5687; J.-R. Shen, *Annu. Rev. Plant Physiol. Plant Mol. Biol.*, 2015, **66**, 23–48.
13 I. D. Young, M. Ibrahim, R. Chatterjee, S. Gul, F. D. Fuller, S. Koroidov, A. S. Brewster, R. Tran, R. Alonso-Mori and T. Kroll, *Nature*, 2016, **540**, 453–457.

14 C. Zhang, C. Chen, H. Dong, J.-R. Shen, H. Dau and J. Zhao, *Science*, 2015, **348**, 690–693.
15 S. Cooper and M. Calvin, *Science*, 1974, **185**, 376–376.
16 W. T. Lee, S. B. Muñoz, D. A. Dickie and J. M. Smith, *Angew. Chem., Int. Ed.*, 2014, **53**, 9856–9859.
17 F. M. Ashmawy, C. A. McAuliffe, R. D. Parish and J. Tames, *J. Chem. Soc., Chem. Commun.*, 1984, 14–16.
18 M. M. Najafpour and D. M. Boghaei, *Transition Met. Chem.*, 2009, **34**, 367–372.
19 M. Watkinson, A. Whiting and C. A. McAuliffe, *J. Chem. Soc., Chem. Commun.*, 1994, 2141–2142.
20 Y. Naruta, M. A. Sasayama and T. Sasaki, *Angew. Chem.*, 1994, **106**, 1964–1965.
21 Y. Naruta, M. a. Sasayama and T. Sasaki, *Angew. Chem., Int. Ed. Engl.*, 1994, **33**, 1839–1841.
22 K. J. Young, B. J. Brennan, R. Tagore and G. W. Brudvig, *Acc. Chem. Res.*, 2015, **48**(3), 567–574.
23 J. Limburg, J. S. Vrettos, L. M. Liable-Sands, A. L. Rheingold, R. H. Crabtree and G. W. Brudvig, *Science*, 1999, **283**, 1524–1527.
24 E. A. Karlsson, B. L. Lee, T. Åkermark, E. V. Johnston, M. D. Kärkäs, J. Sun, Ö. Hansson, J. E. Bäckvall and B. Åkermark, *Angew. Chem.*, 2011, **123**, 11919–11922.
25 Y. Yan, J. S. Lee and D. A. Ruddy, *Inorg. Chem.*, 2015, **54**, 4550–4555.
26 Z. Han, K. T. Horak, H. B. Lee and T. Agapie, *J. Am. Chem. Soc.*, 2017, **139**, 9108–9111.
27 G. Maayan, N. Gluz and G. Christou, *Nat. Catal.*, 2018, **1**, 48.
28 R. K. Hocking, R. Brimblecombe, L.-Y. Chang, A. Singh, M. H. Cheah, C. Glover, W. H. Casey and L. Spiccia, *Nat. Chem.*, 2011, **3**, 461.
29 M. Najafpour, A. N. Moghaddam, H. Dau and I. Zaharieva, *J. Am. Chem. Soc.*, 2014, **136**, 7245–7248.
30 M. M. Najafpour and A. N. Moghaddam, *Dalton Trans.*, 2012, **41**, 10292–10297.
31 A. Singh, R. K. Hocking, S. L.-Y. Chang, B. M. George, M. Fehr, K. Lips, A. Schnegg and L. Spiccia, *Chem. Mater.*, 2013, **25**, 1098–1108.
32 P. Zanello, *Inorganic electrochemistry: theory, practice and application*, Royal Society of Chemistry, 2007.
33 CryAlis PRO, in *Xcalibur R software*, Agilent Technologies, Yarnton, Oxfordshire, England, 2012.
34 G. M. Sheldrick, *Acta Crystallogr.*, 2008, **64**, 112–122.
35 G. M. Sheldrick, *Acta Crystallogr.*, 2015, **71**, 3–8.
36 M. M. Najafpour, N. J. Moghaddam, S. M. Hosseini, S. Madadkhani, M. Hołyńska, S. Mehrabani, R. Bagheri and Z. Song, *Catal. Sci. Technol.*, 2017, **7**, 3499–3510.
37 P. Pedeferri and M. Pourbaix, *Lectures on Electrochemical Corrosion*, 1974.
38 M. Mahdi Najafpour, D. Jafarian Sedigh, S. Maedeh Hosseini and I. Zaharieva, *Inorg. Chem.*, 2016, **55**, 8827–8832.
39 K. Nakamoto and K. Nakamoto, *Infrared and Raman spectra of inorganic and coordination compounds*, Wiley, 1977.
40 D. T. Zahn, *Phys. Chem. Chem. Phys.*, 1999, **1**, 185–190.
41 D. Shevchenko, M. Anderlund, S. Styring, H. Dau, I. Zaharieva and A. Thapper, *Phys. Chem. Chem. Phys.*, 2014, **16**, 11965–11975.
42 M. M. Najafpour, M. Fekete, D. J. Sedigh, E.-M. Aro, R. Carpentier, J. J. Eaton-Rye, H. Nishihara, J.-R. Shen, S. I. Allakhverdiev and L. Spiccia, *ACS Catal.*, 2015, **5**, 1499–1512.

